



BAW
Federal Waterways Engineering
and Research Institute

Rapport de Stage

Quantification of Numerical Uncertainty in Shallow Water Waves

Lucien Le Dimet – 21103896

lucien.le_dimet@etu.sorbonne-universite.fr

M1 Mécanique des Fluides : Fondements et Applications

Advisor : Dr.-Ing. Lahbib Zentari

lahbib.zentari@baw.de

August 30, 2025

Acknowledgements

I would like to express my gratitude to Lahbib Zentari, my advisor, for his unwavering guidance, his careful proofreading of my report, and all the knowledge he shared with me throughout this internship — particularly CFD related - and of course in the art of scientific writing.

I am also sincerely thankful to Carsten Thorenz for his insightful teaching on numerical methods, and to Georg Göbel, from whom I learned a great deal about OpenFOAM. To the whole section „Schiffahrt“ I just want to say: „Hertzlichen Dank!“

Abstract

This study presents a numerical investigation of ship-induced waves in a confined inland waterway, with a focus on assessing the accuracy and reliability of numerical computations through a rigorous Verification and Validation process. The simulation reproduces a full-scale ship navigating the Wesel-Datteln Canal using the interFoam solver in OpenFOAM, with the Volume of Fluid method to capture the free surface and a Reynolds-Averaged Navier–Stokes approach. Several levels of mesh refinement were employed to evaluate discretization errors and assess grid convergence for both scalar and array-type quantities, such as the pressure drag coefficient and free-surface elevation along the hull. While the primary wave field was well captured, the secondary waves proved highly sensitive to mesh resolution, and formal grid convergence was not achieved. Comparison with experimental measurements highlights a good agreement on global wave trends but reveals significant discrepancies of 10% in wave amplitude and temporal stability, underlining the need for finer grids, improved modeling of propeller effects, and potentially the integration of ship dynamics in future work.

Resumé

Cette étude présente une investigation numérique des vagues générées par un navire dans un canal intérieur confiné, avec pour objectif d'évaluer la précision et la fiabilité des calculs numériques à travers un processus rigoureux de vérification et de validation. La simulation reproduit un navire à l'échelle réelle naviguant sur le canal Wesel-Datteln à l'aide du solveur interFoam d'OpenFOAM, en utilisant la méthode VOF pour capturer la surface libre et une approche RANS pour modéliser l'écoulement. Plusieurs niveaux de raffinement de maillage ont été utilisés pour évaluer les erreurs de discréétisation et analyser la convergence du maillage, aussi bien pour des grandeurs scalaires que vectorielles, telles que le coefficient de traînée de pression ou l'élévation de la surface libre le long de la coque. Si le champ de vagues principal a été correctement capturé, les vagues secondaires se sont révélées très sensibles à la résolution du maillage, et une convergence formelle n'a pas pu être atteinte. La comparaison avec les mesures expérimentales montre une bonne concordance sur les tendances globales des vagues, mais révèle des écarts significatifs pouvant atteindre 10% sur l'amplitude et la stabilité temporelle des vagues, soulignant ainsi la nécessité de maillages plus fins, d'une modélisation améliorée des effets d'hélice, et potentiellement de l'intégration de la dynamique du navire dans les travaux futurs.

Contents

1	Introduction	4
2	Theoretical Background	6
2.1	Ship induced waves in confined waters and propulsion effects	6
2.2	Mathematical notations and numerical procedure	7
2.2.1	Governing equations	7
2.2.2	Solver	8
2.3	Numerical Errors and Uncertainties	8
2.4	Extrapolation of Grid-Independent Solution for a Scalar Quantity	9
3	Computational Setup	11
3.1	Ship and Canal Characteristics	11
3.2	Numerical Discretization Schemes and Linears Solvers	11
3.3	Boundary conditions	12
3.4	Meshing Strategy	13
4	Verification and Validation.	17
4.1	Iterative convergence	17
4.2	Statistical convergence	18
4.3	Extrapolation of grid independent solutions	19
4.3.1	Grid independent solution of a scalar quantity	19
4.3.2	Grid independent solution of an array-type quantity	20
4.4	Spatial and temporal Fourier analysis	21
4.5	Validation	23
5	Conclusion	27
References		28

1 Introduction

Accurate prediction of ship-generated waves plays a crucial role in estimating the potential damage to canal banks. As mentioned in Duró et al. 2020, repeated wave impacts can lead to significant erosion of the riprap layer and the underlying soil, compromising the structural integrity of the waterway. Thus, accurately quantifying wave heights provides essential input for predicting bank degradation and for designing more resilient bank protection systems. This is particularly important in artificial waterways such as the Wesel-Datteln Kanal (WDK), where maintaining navigability and minimizing maintenance costs are critical priorities. In this context, both experimental and numerical studies provide key information to quantify the effects of ship-generated waves. Here, Computational Fluid Dynamics (CFD) plays a key role by enabling detailed simulations of ship-waterway interactions, complementing field measurements and allowing for the exploration of a wide range of operating scenarios. Experimental data are essential to validate appropriate numerical methods; thus, both approaches are complementary and necessary.

For this purpose, the German Federal Waterways Engineering and Research Institute (Bundesanstalt für Wasserbau, BAW) carried out an extensive measurement campaign on the WDK in 2004. An inland waterway ship of 110 m length navigated a straight, uniform reach of the canal at various speeds and distances from the bank. The ship-generated wave height was measured using an ultrasonic probe positioned midway up the bank. Recently, these results were used by Göbel et al. 2023 to perform a comparison of ship-generated wave height prediction using different numerical methods. They highlighted the complexity of the numerical prediction of shallow water waves in confined environments. Above all, in their study, it became apparent that a thorough *Verification* and *Validation* (*V&V*) exercise is necessary to ensure that the numerical methods are working as intended. The *Verification* process consists of ensuring that the numerical solver works well (discretization error, convergence, iteration, solving the right physics, etc.). The *Validation* process consists of comparing numerically obtained results with measurements, thus ensuring that the modeling error stays below an acceptable margin.

While experimental uncertainty in measurement campaigns is often easier to quantify, as it is typically based on sensor accuracy and measurement repeatability, quantifying the numerical error requires the development of a thorough *V&V* procedure. Indeed, numerical errors of even a few percent can result in substantial economic consequences, especially when informing large-scale engineering decisions. The need for accurate error estimation is thus crucial when performing numerical simulations. This is largely emphasized in foundational literature, most prominently by Ferziger et al. 2019. Regarding numerical methods applied to ship hydrodynamics, Eça and Hoekstra 2014; Oberhagemann and el Moctar 2019; Xing and Stern 2010 all provide reliable estimators of numerical errors. Here, grid convergence studies are typically carried out by considering one integral quantity, such as ship resistance, split into frictional resistance and wave-making resistance. For instance, Descamps et al. 2025 focused on the wave resistance coefficient as a validation metric, among others. In Pereira et al. 2017, the convergence of friction and pressure coefficients is assessed; in Islam and Guedes Soares 2019, an uncertainty analysis is performed on the total resistance coefficient, sinkage, and trim of a merchant ship.

The studies cited above all assess grid convergence by only considering one integral, ship-centric quantity of interest. In the present study, we shifted our focus from consider-

ing quantities of interest from a ship-centric perspective to an environmental hydraulics perspective. In this regard, the pressure and velocity variations induced by ship-generated waves are the key metrics we considered. As such, we applied the grid uncertainty procedure by Oberhagemann and el Moctar 2019 to extract a grid-independent array-type quantity: the wave elevation alongside the hull. For this purpose, we paid particular attention to the numerically obtained free-surface elevation in the vicinity of the ship. In the present study, we reproduced the case described by Göbel et al. 2023: a typical 110 m inland waterway ship, sailing straight-ahead in a confined channel, the WDK. Here, we developed a thorough *V&V* exercise considering a multi-phase numerical simulation using the open-source CFD toolbox OpenFOAM. We performed the simulations using three successively refined grids and extracted a grid-independent solution for the ship-generated wave using the procedure by Oberhagemann and el Moctar 2019. We validated our results using the full-scale measurement performed by BAW in 2004. Our study revealed that estimating the grid convergence using an array-type quantity of interest is highly sensitive to grid-resolution, spatial and temporal discretizations. Our study is structured as follows:

- Section 2 introduces briefly the theoretical background, including basic physical mechanisms behind ship waves, relevant mathematical formulations, and the numerical approach employed.
- Section 3 details the computational setup, including boundary conditions, domain configuration, and the meshing strategy used for the simulations.
- Section 4 focuses on validation and verification procedures, covering convergence studies, error analysis, Fourier analysis, and validation.
- Finally, Section 5 summarizes the key findings and outlines possible directions for future work.

2 Theoretical Background

2.1 Ship induced waves in confined waters and propulsion effects

As a ship moves through water, it displaces the surrounding fluid, creating a backward current along its sides and thus lowering pressure, which causes a lateral drop in water level (the red area in 1 schematizes this phenomenon). Stagnation points at the bow and stern lead to local pressure increases, resulting in a bow wave, a trough along the hull, and a stern wave from a stationary observer's view, as it is schemed in 2. According to Lataire et al. 2012, flow acceleration beneath the hull leads to a pressure drop that increases squat, characterized by hull sinkage and trim. This effect is intensified in constrained environments due to reduced cross-sectional area, particularly when the waterway is confined or shallow relative to the ship. According to Du et al. 2020, confinement effects become significant when the ratio of waterway width to ship breadth falls below 15–20; in our case, this ratio is only 4.8. Shallow water effects typically begin to be important when the ratio of water depth to ship draft is between 1.5 and 2, while our configuration yields a ratio of 1.26. As the under-keel clearance decreases, axial inflow toward the propeller becomes increasingly accelerated. The propeller reinforces this effect by drawing water from beneath the hull, producing a pronounced low-pressure region at the stern. This suction not only intensifies the axial flow but also exerts a downward force on the hull, further increasing stern trim and total squat (Raza et al. 2025).

Figures 1 and 2 illustrate the influence of shallow water effects on ship dynamics, highlighting changes in water surface elevation, ship motion, and flow characteristics.

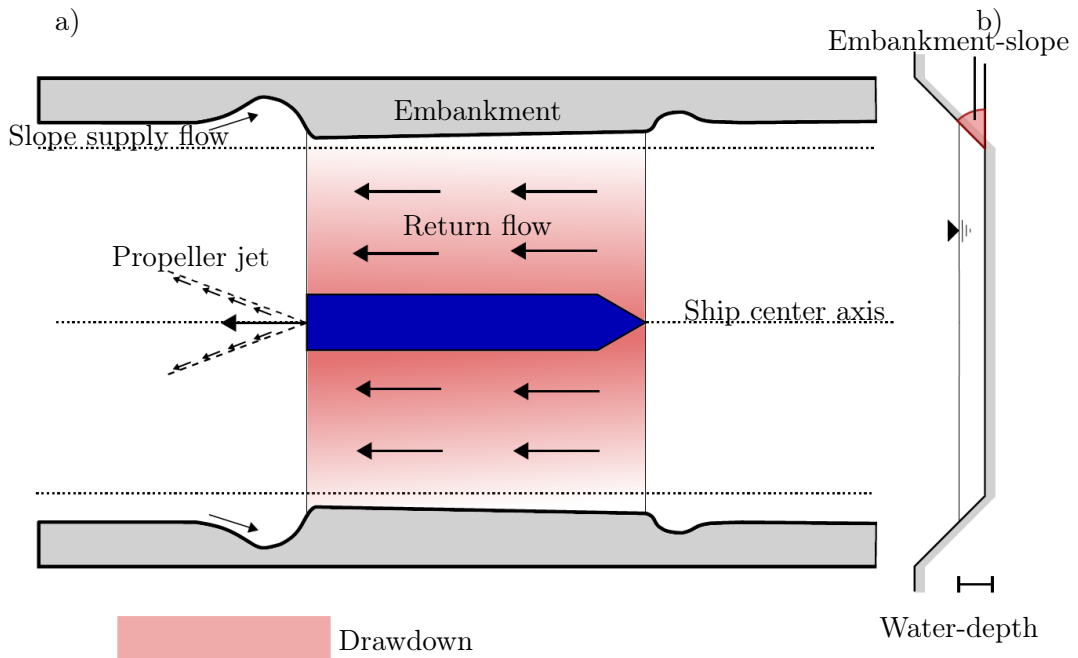


Figure 1: Schematic of the ship wave induced currents in a trapezoidal channel. a) top view and b) cross-section. The area highlighted in red indicates the drawdown (Reproduced from Dempwolff et al. 2022)

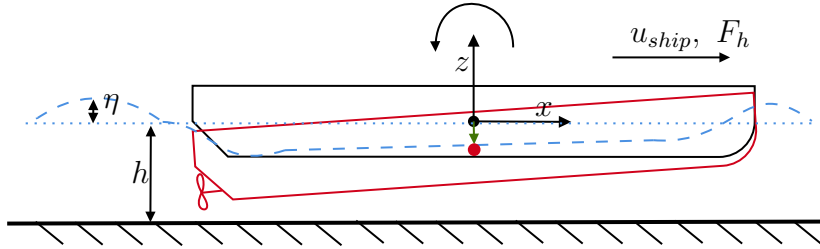


Figure 2: Sketch illustrating the behavior of a ship in shallow water. The dotted blue line represents the water depth h , while the free surface elevation is denoted by η , and the ship-induced water level is shown in dashed blue. The black ship indicates the stationary configuration, whereas the red ship illustrates the effects of shallow water dynamics. The ship speed is indicated by u_{ship} , and the depth Froude number F_h .

2.2 Mathematical notations and numerical procedure

The purpose of our analysis was to quantify the grid uncertainty in shallow-water waves simulations using numerical flow simulations. In this section, we thus briefly introduce the governing equations used to solve our problem.

2.2.1 Governing equations

The governing equations in this case are the 3-D incompressible and isothermal Navier-Stokes equations. To account for turbulence effects, these equations are modeled using the Reynolds-Averaged Navier-Stokes (RANS) approach, which involves statistical averaging and additional modeling assumptions. The RANS equation reads:

$$\partial_t \bar{u}_i + \bar{u}_j \partial_j \bar{u}_i = -\frac{1}{\rho} \partial_i \bar{p} + \nu \partial_{jj} \bar{u}_i - \partial_j \bar{u}'_i \bar{u}'_j \quad (2.1)$$

Where: \bar{u}_i is the Reynolds-averaged velocity component, \bar{p} the mean pressure and $\bar{u}'_i \bar{u}'_j$ is the Reynolds stress tensor, which needs to be modeled.

For this purpose, the two-equation closure model $k-\omega$ SST, as detailed in Menter 1994, is well-suited for our case since it combines the near-wall accuracy of the $k-\omega$ formulation with the freestream robustness of the $k-\varepsilon$ model, enabling reliable predictions in both boundary layers and separated flow regions. Its ability to capture adverse pressure gradients and flow separation makes it particularly appropriate for simulating ship-induced flows as detailed in Pena and Huang 2021.

Our case deals with free surface problems. Hence, we relied on the Volume of Fluid (VoF) method (see Hirt and Nichols 1981; Nichols et al. 1980) to resolve the water and air phases. The VoF method handles multiphase flow as a single continuum with spatially varying properties and an interface between both. The local mass distribution between air and water is quantified by α ranging from 0 to 1. The density ρ and viscosity μ are defined as such:

$$\rho = \alpha \rho_w + (1 - \alpha) \rho_a \quad (2.2a)$$

$$\mu = \alpha \mu_w + (1 - \alpha) \mu_a \quad (2.2b)$$

Where the indexes w and a denote the water and air phases, respectively. An additional equation is solved to account for the interface transport:

$$\partial_t \alpha + \nabla(\alpha \mathbf{u}) = 0 \quad (2.3)$$

A key criterion to ensure proper functioning of the VoF algorithm is the Courant-Friedrichs-Lowy (CFL) number criteria. It indicates the ratio of velocity and timestep to grid spacing for a single cell. The CFL number is defined as:

$$\text{CFL} = \frac{u \Delta t}{\Delta x} \quad (2.4)$$

Where: u is the local flow velocity (m/s), Δt is the time step (s) and Δx is the spatial grid size (m).

For free-surface flow, a mean CFL number on the free surface of 0.5 is considered good practice, as it ensures a time-steps small enough to allow an accurate transport of quantities between one cell and another.

2.2.2 Solver

We relied on the open source solver OpenFOAM for our simulations. It is an open-source C++ library designed for solving systems of partial differential equations, see (Weller et al. 1998). It provides a wide range of solvers tailored to specific physical phenomena. Among them, `interFoam` is a two-phase flow solver for simulating free surface flows, based on the (VoF) method. The mass and momentum conservation equations are solved using the PIMPLE algorithm, which combines the Semi-Implicit Method for Pressure-Linked Equations (SIMPLE) and Pressure-Implicit with Splitting of Operators (PISO) methods for pressure–velocity coupling. The distribution of air and water transport equation is solved using OpenFOAM’s MULES (Multidimensional Universal Limiter for Explicit Solution) algorithm. In this work, OpenFOAM version 2412 is used.

Within `interFoam` the pressure is defined as: $p_{rgh} = p - \rho gh$. Separating the hydrostatic pressure contribution from the dynamic pressure field improves numerical stability and facilitates the treatment of the free surface.

2.3 Numerical Errors and Uncertainties

As discussed in Ferziger et al. 2019, during numerical simulations, several types of errors may arise from different sources: ϵ_M denotes the modeling error, ϵ_d the discretisation error, ϵ_I the input uncertainty, ϵ_{ro} the round-off error, and ϵ_{st} the statistical error. So the total computational error ϵ_T of a quantity reads:

$$\epsilon_T = \epsilon_M + \epsilon_I + \epsilon_{NS} \quad (2.5)$$

Where the numerical simulation error ϵ_{NS} is defined as:

$$\epsilon_{NS} = \epsilon_{ro} + \epsilon_{it} + \epsilon_d + \epsilon_{st} \quad (2.6)$$

For the purpose of validation, modeling errors ϵ_M are of primary importance, whereas verification focuses on numerical simulation errors ϵ_{NS} , as mentioned in Eça and Hoekstra 2009. ϵ_M , the modeling error, quantifies the discrepancy between the real physical flow and the mathematical model used to represent it.

The round-off error ϵ_{ro} corresponds to the difference between a computed numerical value and its exact mathematical counterpart. In double-precision computations (i.e., using 16 significant digits), round-off errors are typically negligible (see Eça and Hoekstra 2009).

The discretization error ϵ_d is defined as the deviation between the exact solution of the continuous conservation equations and the solution of the corresponding discretized (spatial and temporal) algebraic system.

The iterative error ϵ_{it} arises from the difference between the exact and the numerically converged solutions of the algebraic system. This error is typically controlled via the residual levels. If the residuals are reduced by at least two orders of magnitude below the discretization error, the iterative error can generally be considered negligible, leaving the discretization error as the dominant component of the numerical error (Eça and Hoekstra 2009).

In unsteady flow problems, statistical errors ϵ_{st} also play a significant role. These errors arise from the finite size of the computational domain and the limited duration of the simulation. Although they can be reduced by performing multiple simulations and averaging the results, such approaches are computationally expensive. Therefore, accurate error estimates that do not rely on repeated simulations are essential for practical engineering applications as it is emphasized in Brouwer et al. 2015. Finally, the input error ϵ_I , also referred to as "programming and user errors" in Ferziger et al. 2019, refers to issues such as bugs in the code or incorrect implementation of boundary conditions.

In this report, we will focus on quantifying the grid uncertainty which stems mostly from ϵ_d . The experimental data will allow us to evaluate both ϵ_I and ϵ_M .

2.4 Extrapolation of Grid-Independent Solution for a Scalar Quantity

Let us consider a scalar quantity ϕ_i , where ϕ_1 , ϕ_2 , and ϕ_3 correspond to the solutions obtained using fine, medium, and coarse grid resolutions, respectively, as described in Eça and Hoekstra 2014.

In Eça and Hoekstra 2014, the convergence ratio R is estimated as :

$$R = \frac{\phi_2 - \phi_1}{\phi_3 - \phi_2} \quad (2.7)$$

And the convergence conditions are:

- Monotonic convergence: $0 < R < 1$
- Monotonic divergence: $R > 1$
- Oscillatory convergence: $R < 0$ and $|R| < 1$
- Oscillatory divergence: $R < 0$ and $|R| > 1$

The method by Oberhagemann and el Moctar 2019, requires uniform refinement in all spatial dimensions as well as time to achieve constant Courant numbers. In Oberhagemann and el Moctar 2019, a non-dimensional scalar grid refinement ratio Υ is defined with:

$$\Upsilon = \sqrt{\frac{1}{2} \left(\left(\frac{\Delta x_i}{\Delta x_3} \right)^2 + \left(\frac{\Delta y_i}{\Delta y_3} \right)^2 + \left(\frac{\Delta z_i}{\Delta z_3} \right)^2 \right)} \quad (2.8)$$

Where x_i , y_i and z_i are the base cell size dimensions. The coarsest grid is defined as the reference grid. So the smallest known Υ value is 0.5, while the largest one is 1 and the

grid-independent solution reads: $\phi_0 = \Phi(\Upsilon = 0)$. In our case, $\Phi(\Upsilon)$ a polynomial fitted to the results at multiple grid levels, is computed using least square minimization as it is proposed in Eça and Hoekstra 2014. It can be practical to give more value to the finer than the coarser grids, therefore, it is possible to obtain the least square estimators with weights:

$$S_{RE}^W(\phi_0, \alpha, p) = \sqrt{\sum_{i=1}^{n_g} w_i (\phi_i - (\phi_0 + \alpha h_i^p))^2} \quad (2.9a)$$

$$S_1^W(\phi_0, \alpha) = \sqrt{\sum_{i=1}^{n_g} w_i (\phi_i - (\phi_0 + \alpha h_i))^2} \quad (2.9b)$$

$$S_2^W(\phi_0, \alpha) = \sqrt{\sum_{i=1}^{n_g} w_i (\phi_i - (\phi_0 + \alpha h_i^2))^2} \quad (2.9c)$$

$$S_{12}^W(\phi_0, \alpha_1, \alpha_2) = \sqrt{\sum_{i=1}^{n_g} w_i (\phi_i - (\phi_0 + \alpha_1 h_i + \alpha_2 h_i^2))^2} \quad (2.9d)$$

$$w_i = \frac{1/h_i}{\sum_{i=1}^{n_g} 1/h_i} \quad (2.9e)$$

Where p is the observed order of grid convergence, $\alpha, \alpha_1, \alpha_2$ are the fitting coefficients and h_i is the typical grid cell size. A non-weighted approach can also be derived from 2.9 with $w_i = 1$. Then, the discretization error δ_D is estimated with:

$$\epsilon_d \approx \delta_D = \phi_i - \phi_0 \quad (2.10)$$

In this report, we employed the Oberhagemann and el Moctar 2019 method to quantify a scalar quantity as well as an array-type quantity.

3 Computational Setup

3.1 Ship and Canal Characteristics

The simulation setup is based on a full-scale inland waterway ship navigating the WDK. The main geometrical and hydrodynamic properties of the ship and the canal are summarized in Table 1. In this table, the trim angle denotes the rotation about the y -axis in the positive (trigonometric) direction while CoG refers to the Center of Gravity of the ship. The depth Froude number is defined as $F_h = u_{\text{ship}}/\sqrt{gh}$ while the length-based Reynolds number is given by $Re_{L_{pp}} = u_{\text{ship}}L_{pp}/\nu$, where u_{ship} is the ship velocity, h is the water depth, L_{pp} is the length between perpendiculars, g is the gravitational acceleration, and ν is the kinematic viscosity. At 20°C, the kinematic viscosity of water is approximately $\nu \approx 1.0 \times 10^{-6} \text{ m}^2/\text{s}$.

Table 1: Main physical properties of the ship and canal configuration.

Category	Quantity	Value
Ship	Length between perpendiculars, L_{pp}	105 m
	Beam, B	11 m
	CoG draft, T	3.16 m
	Froude number, F_h	0.406
	Reynolds number, $Re_{L_{pp}}$	2.7×10^8
	Trim angle	-0.044°
Canal	Roughness Hull, k_s^{hull}	0.003 m
	Water depth, h	3.95 m
	Width at free surface	52.6 m
	Gravel bed width	33.4 m
	Bank slope	1:2.43
	Roughness (slope/bed), $k_s^{\text{slope}} / k_s^{\text{bed}}$	0.3 m / 0.03 m

3.2 Numerical Discretization Schemes and Linears Solvers

In our simulation, we solve for pressure, velocity and turbulent quantities. The transport equations mentioned in 2.2.1 are solved using the following algorithms, as implemented in OpenFOAM. Table 2 summarizes the time and spatial discretization schemes used for the different equations. A backward Euler scheme (B-E) is applied for time integration. Flux limiters are employed in the spatial schemes to ensure numerical stability and to prevent spurious oscillations, particularly near sharp gradients or at the interface.

Table 2: List of the discretization schemes used. [blue](#) terms identifies in-house schemes, B-E stands for Backward Euler

Solved eq.	Time scheme	Spatial scheme
Momentum	B-E	Gauss linearUpwind (2^{nd} order, Face Gradient limiter)
Turbulence	B-E	Gauss CoBlended (van Leer & Minmod flux limiters)
VoF convection	B-E	Gauss (vanAlbada flux limiter)

Table 3 presents the various iterative linear solvers. **DILUPBiCGStab** stands for Diagonal Incomplete LU Preconditioned BiConjugate Gradient Stabilized while **GAMGPBiCGStab**, stands for Geometric Agglomerated Algebraic MultiGrid Preconditioned Bi-Conjugate Gradient Stabilized (see van der Vorst 1992).

Table 3: Linear solvers used in the case.

Solved eq.	Linear solver
VoF	DILUPBiCGStab
Momentum Predictor	DILUPBiCGStab
PISO loop	GAMGPBiCGStab
Turbulence (k & ω)	GAMGPBiCGStab

3.3 Boundary conditions

Figure 3 presents a schematized view of the computational domain. Here, we list the boundary conditions, summarized in table 4. The top of the domain was assigned a symmetry condition except for the dissipation rate ω as it was found that a Neumann condition lowered the overall turbulence of the air phase thus leading to an overall sharper interface. The bottom of the canal, the side walls as well as the ship's hull were assigned a no-slip wall condition. The front of the canal, placed approximately one ship length on front of the bow, was assigned an inlet condition, and finally, the back of the canal, placed approximately 3 ship lengths behind the stern of the ship, was assigned an outlet condition. Table 4 lists all the boundaries as well as the corresponding boundary condition for each quantity of interest. In this table, we introduce the term **wF** or "wall function". It denotes the use of semi-empirical formulas used to bridge the near-wall region of a turbulent boundary layer without the need to fully resolve it down to the viscous sub-layer. This approach is essential in full-scale simulations where resolving the entire boundary layer would require extremely fine meshes — too fine to be computationally affordable. Defining y^+ a non-dimensional number:

$$y^+ = \frac{u_\tau y}{\nu} \quad (3.1)$$

Where u_τ is the friction velocity, y the normal distance between the wall and any cell node. Since viscous forces around the hull are not of primary interest, we target a y^+ value of approximately 300 to remain in the fully rough turbulent regime. More details are provided in Ferziger et al. 2019.

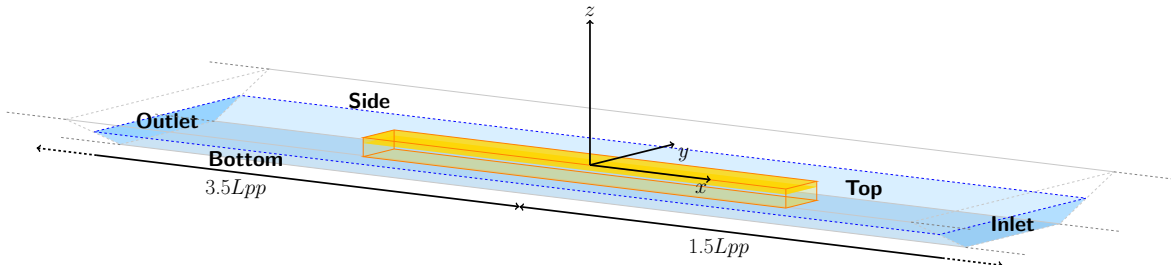


Figure 3: Three-dimensional view of the computational domain, where the bottom and side surfaces correspond to sections of the canal and are differentiated by varying roughness characteristics (see 1 for the corresponding values).

Table 4: Boundary conditions (BCs) used in the `interFoam` simulation. D and N denote Dirichlet and Neumann BCs, respectively; D/N indicates a mixed condition, C indicates a calculated BC computed from internal field values, wF a wall function. **red** terms identifies the use an in-house function.

Field	Inlet	Outlet	Top	Canal	Hull
velocity \mathbf{u}	D	D	N	D	wF
volume fraction α	D	N	N	N	N
p_{rgh}	C	C	C	C	N
turbulent kin. enr. k	D	D	wF	wF	wF
dissip. rate ω	D	D	N	wF	wF
turbulent kin. visc. ν_t	C	C	C	wF	wF

Regarding propulsion effects, an in-house propeller model is employed to simulate the hydrodynamic influence of the propeller on the surrounding flow field.

3.4 Meshing Strategy

As the results strongly depend on mesh quality and refinement, the following meshing strategy was adopted. Three meshes are required to apply the method described in Oberhagemann and el Moctar 2019. Each mesh consists of base cells (`level 0`), which are recursively subdivided into 8 child cells of `level i+1` following the octree method. A refinement factor of $\sqrt{2}$ is applied to the base cell size between each successive mesh. Table 5 summarizes the main characteristics of the three meshes used for the grid convergence study.

Figure 4 displays a cross-section of the internal mesh at the horizontal plane $z = 0$ m. Figure 5 provides close-up views of the surface mesh at both the stern and bow across the three mesh refinement levels. In addition, Figure 6 presents a three-dimensional perspective of these surface mesh regions.

Figures 7, 8 and 9 show mesh detailed cross-sections of the internal mesh, along the three planes: $y = 0$ m, $x = -48, 50$ m and $z = 0$ m.

Mesh stretching was used to gradually increase the cell size in the downstream region behind the ship. This reduces the numerical resolution where wave details are less important, helping to dissipate wave energy and lowering computational cost. The **red** box in figure 9 highlights the region where the mesh-stretching strategy is applied.

Figure 8 and 9 show that the mesh surrounding the hull includes 2 distinct levels of refinement, as detailed in Table 5. A `level 5` refinement box in **green** is located around the stern of the ship to match the complex geometry which is particularly noticeable in the left picture of 6 (also seen in 7, 9 and 8). Cells surrounding the hull are kept at `level 4` up to the bank, ensuring minimal numerical wave damping.

An anisotropic refinement layer is applied throughout the computational domain near the free surface, highlighted in **blue** in Figure 7. This region, refined to `level 4` in the vertical (z) direction between $z = -0.6$ m and $z = 0.6$ m, enables accurate resolution of the free-surface waves. Maintaining sufficient resolution at the interface is critical, as coarse cells can introduce artificial wave damping and obscure secondary wave features. Furthermore, excessive refinement or coarsening in the z direction at the air-water interface can lead to steep α gradients, resulting in inaccuracies in free-surface representation.

Table 5: The refinement levels associated with each mesh resolution are summarized below. The characteristic grid size is expressed in meters. In this octree-based approach, a cell at level i is subdivided into 8 child cells at level $i + 1$.

Mesh	Base mesh	level 1	level 2	level 3	level 4	level 5	N_{cells}
Coarse	4	2	1	0.5	0.25	0.125	2 mio
Medium	2.82	1.41	0.705	0.3525	0.17625	0.088125	6 mio
Fine	2	1	0.5	0.25	0.125	0.06125	16 mio

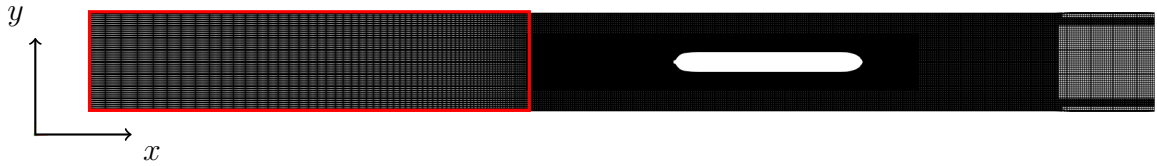


Figure 4: 2D cross-section at $z = 0$. **Mesh stretching** is applied downstream of the ship dissipating the waves.

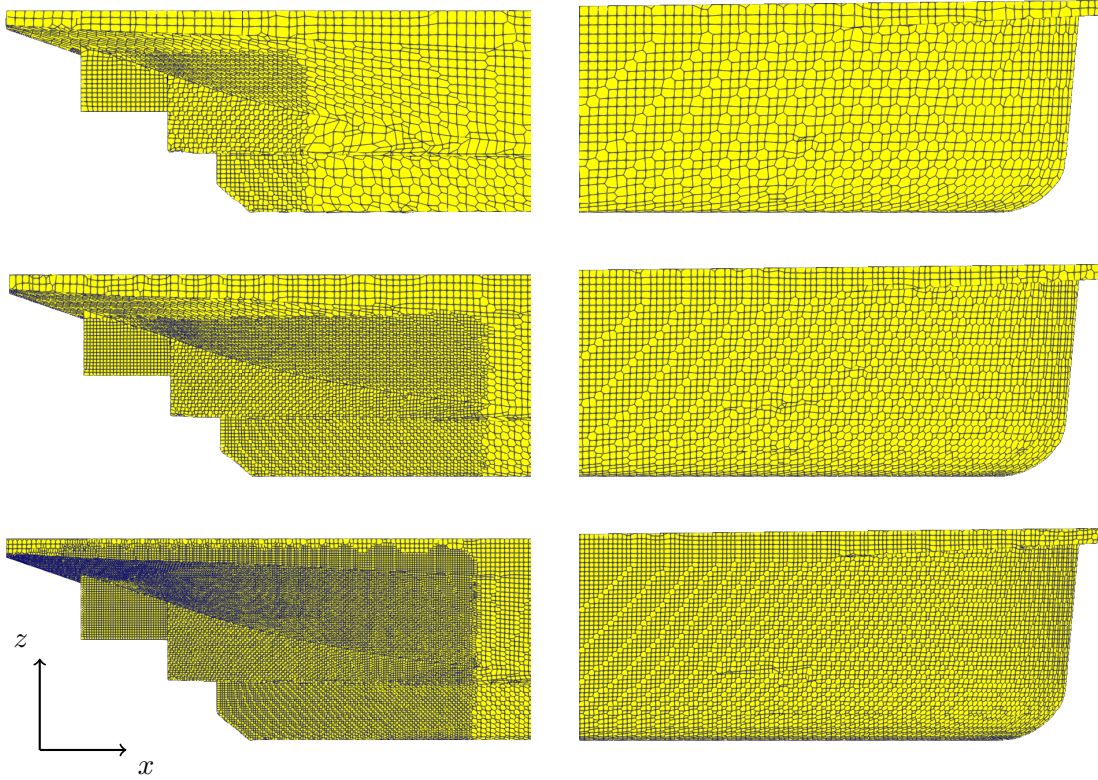


Figure 5: Coarse, medium, and fine mesh views of the ship, from top to bottom. Each row shows aft (left) and bow (right) perspectives.

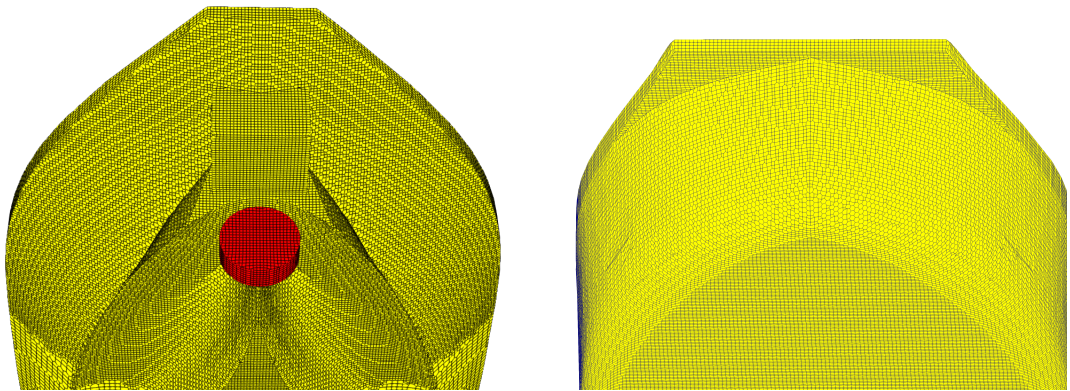


Figure 6: Fine mesh, 3-D views of the surface meshes of the stern (left) and the bow (right), the propeller is visible in red.

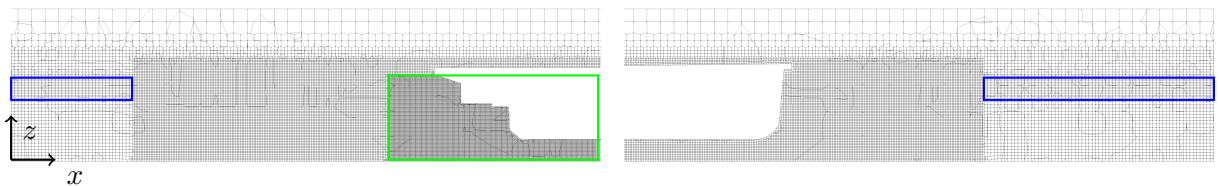


Figure 7: Fine mesh cross-sections taken at $y = 0$, left shows the aft region of the hull, right shows the bow. blue zones show anisotropic mesh refinement around the free-surface, green rectangle show the very fine refinement around the stern to match the complex geometry (see 6)

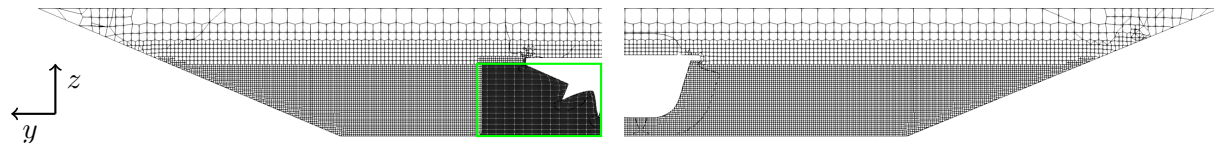


Figure 8: Fine mesh cross-sections left shows the aft region of the hull, taken at $x = -48 \text{ m}$, right shows the bow taken at $x = 50 \text{ m}$.

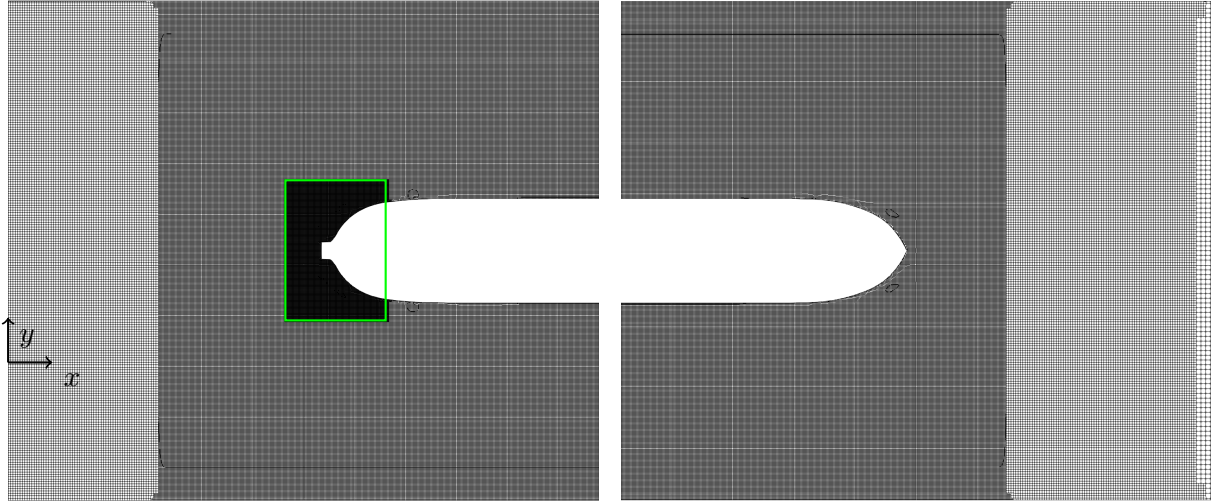


Figure 9: Fine mesh cross-sections taken at $z = 0$, left shows the aft region of the hull, right shows the bow. green rectangle show the very fine refinement around the stern to match the complex geometry (see 8)

The highest CFL number was kept under 4 throughout the various cases, with adaptive time stepping, with the following mean (across the domain) Courant numbers: $\bar{CFL}^{Fine} = 0.053$, $\bar{CFL}^{Medium} = 0.039$ and $\bar{CFL}^{Coarse} = 0.031$.

Overall, the meshing strategy was designed to balance computational efficiency and wave resolution accuracy, with particular attention to the free surface and the complex hull geometry.

4 Verification and Validation.

As emphasized by Ferziger et al. 2019, reliable CFD results require both iterative convergence, ensuring residuals drop sufficiently at each timestep below a threshold, and statistical convergence, ensuring time-averaged quantities stabilize over the simulation duration.

This section details the criteria and methods for assessing both convergence types. This exercise was performed on the medium mesh. In this study, all meshes considered for our grid uncertainty analysis met the quality requirements.

4.1 Iterative convergence

The iterative solver settings in `interFoam` are critical, particularly for unsteady simulations. The PIMPLE algorithm combines the outer iterations of SIMPLE with the inner correctors of PISO to enhance pressure–velocity coupling. In this framework, each outer iteration addresses momentum equation convergence, while the inner PISO loops enforce mass conservation through repeated pressure corrections. The accuracy of the outer loops is assessed based on the magnitude of the residuals from the iterative linear solvers. Here, we used the L_2 Norm to evaluate the residuals. Within openFoam, the L_2 norm is defined as such:

$$L_2 = \sqrt{\frac{1}{N} \sum_{i=1}^N R_i^2} \quad (4.1)$$

Where R is the residual of the linear solver and N the matrix size. Figure 10 shows the initial L_2 residuals for p_{rgh} , $\|U\|_\infty = \max\{ \|u\|_2, \|v\|_2, \|w\|_2 \}$ and Continuity. According to Eça and Hoekstra 2009, outer iterations should reduce residuals by at least two orders of magnitude in unsteady simulations which is the case here with 3 outer iterations. Three inner iterations were sufficient to ensure numerical stability.

Figure 11 presents the L_2 residuals as a function of the number of iterations for the coarse case. The residual convergence was consistent throughout the simulation which shows a well-converged case.

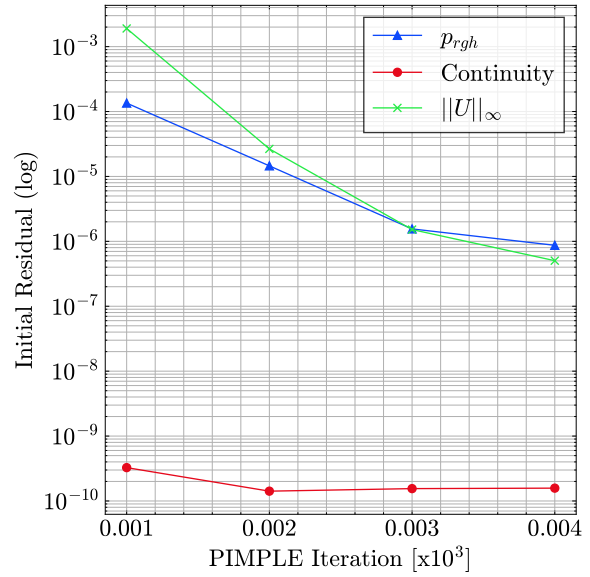


Figure 10: L_2 residuals over 4 PIMPLE iterations.

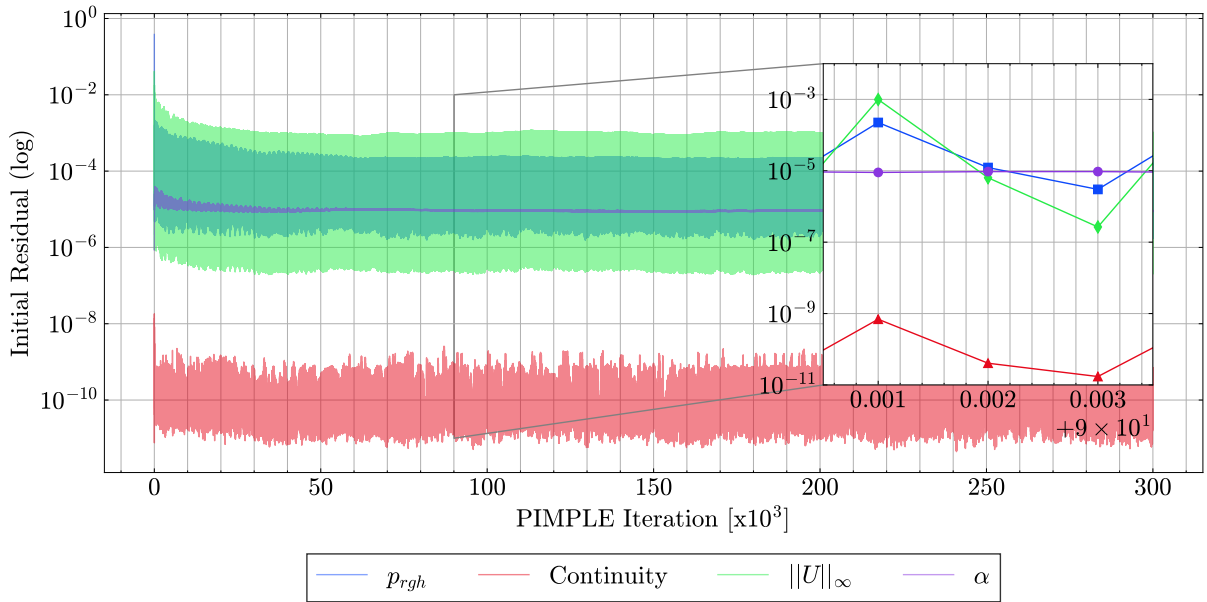


Figure 11: Iterative convergence of the L_2 residuals of: α , p_{rgh} and the L_∞ norm of the velocity vector as well as the continuity error made at each iteration. The inset shows the three PIMPLE iterations per time step. The residuals demonstrate steady convergence.

4.2 Statistical convergence

From an engineering point of view, a ship traveling in calm water at a constant speed may be considered as a quasi-steady problem. Indeed, in speed power predictions, one ship velocity correspond to one resistance value, averaged in time. However, to ensure the value is corrected, the mean of this value should be constant in time. Similarly, in our case, we aimed for quasi-steady solution to obtain a time averaged free-surface elevation for one ship speed. Thus, statistical convergence must be verified on wave elevations along the hull. We considered a solution as statistically converged when the mean value of a given quantity did not vary under a specified threshold for approximately 100 seconds.

The statistical convergence is presented in figure 12. The mean water level $\bar{\eta}$ was computed from the pressure field at $z = -0.75$ m allowing for a small damping of surface wavelets. Mean values $\bar{\eta}_{200}$ and $\bar{\eta}_{100}$ are computed for two periods of time: 200 and 100 seconds. $\bar{\eta}_{200}$ was chosen as the reference. The relative deviation was computed as:

$$\delta_i^{Case} = \frac{|\bar{\eta}_i - \bar{\eta}_{200}|}{|\bar{\eta}_{200}|}. \quad (4.2)$$

The relative deviation reads: $\delta_{100}^{Fine} = 0.4\%$ thus, we can conclude that the fine case was well converged over time. Medium and coarse present the same behaviors: $\delta_{100}^{Medium} = 0.17\%$ and $\delta_{100}^{Coarse} = 0.25\%$. The fine case presents an unsteady behavior for the first 800 seconds as it was run without any initialization. Medium and coarse cases were initialized using the fine case which was appreciable in their overall steadier behavior.

This plot illustrates that this case is quasi-steady. Thus, the grid-convergence procedures 2.4 are applied to quantities averaged over the final 100 s of each run.

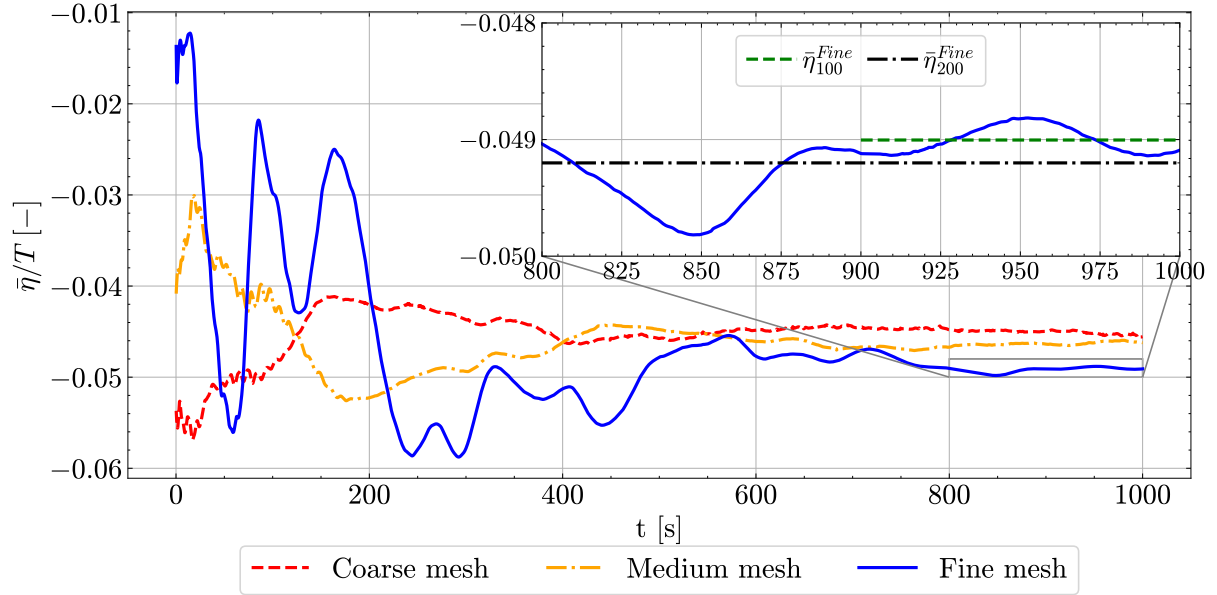


Figure 12: Mean value of the water level across the whole domain, $\bar{\eta}$ as a function of time. $\bar{\eta}_{100}$ and $\bar{\eta}_{200}$ represent the mean values of the water level during 100 and 200 seconds, respectively. This figure shows that the cases tend to a steady-state behavior

4.3 Extrapolation of grid independent solutions

To assess ϵ_d , the discretization error, and to quantify the uncertainty introduced by the mesh resolution, a grid convergence study was performed. This section focuses on extrapolating grid-independent solutions using Richardson extrapolation to evaluate how numerical results evolve with mesh refinement. The first subsection applies the method to scalar quantities, while the second extends the analysis to array-type quantities.

4.3.1 Grid independent solution of a scalar quantity

Using the method of Oberhagemann and el Moctar 2019, as described in 2.4, we extrapolated a grid independent solution using S_1 and S_2 (non-weighted polynomials, *ie.* $w_i=1$) for the coefficient of total pressure drag as well as the mean water level elevation. The coefficient of total pressure drag is defined as such: $C_{T_P} = \frac{D_P}{0.5\rho U^2 S_w}$ where D_P is the mean drag force due to pressure forces, ρ the water density, U the ship velocity and S_w is the wetted hull area. As mentioned in 4.2 the value of C_{T_P} is averaged over the last 100 seconds of the simulation. The figure 13 details this analysis: the quantities of interest are computed on various grids for and expressed as a function of Υ , the non dimensional cell-size.

In our case, we considered three successively refined grids, ranging from fine to coarse. The coarse grid comprised 2 millions cells (ϕ_3), the medium grid 6 millions (ϕ_2) and the fine grid 16 millions (ϕ_1) cells, as detailed in table 5.

The convergence ratios where obtainment using equation 2.7. For C_{T_P100} this ratio was $R = -1.043$, showing an oscillatory divergence by a small margin while for $\bar{\eta}_{100}$, the ratio reads $R = 2.556$, thus demonstrating a monotonous divergence. Nevertheless, the Oberhagemann and el Moctar 2019 methods yields an extrapolated solution, despite a diverging behavior. The grid uncertainty error is defined as the percentage difference between the obtained value of a quantity ϕ_i on a grid i and the extrapolated solution ϕ_0

calculated using a polynomial S_j as detailed in 2.9:

$$\delta_D^{S_j} = \frac{|\phi_i - \phi_0|}{\phi_0} [\%].$$

Table 6 quantifies the error assessed with each quantity of interest. Notably, the pressure drag coefficient error is smallest on the coarse grid, whereas the free-surface error is smallest on the fine grid. This underscores that the free-surface elevation is more sensitive to grid resolution. This highlights that the free surface is mostly sensible to grid resolution, which amplifies unsteady effects near the free surface.

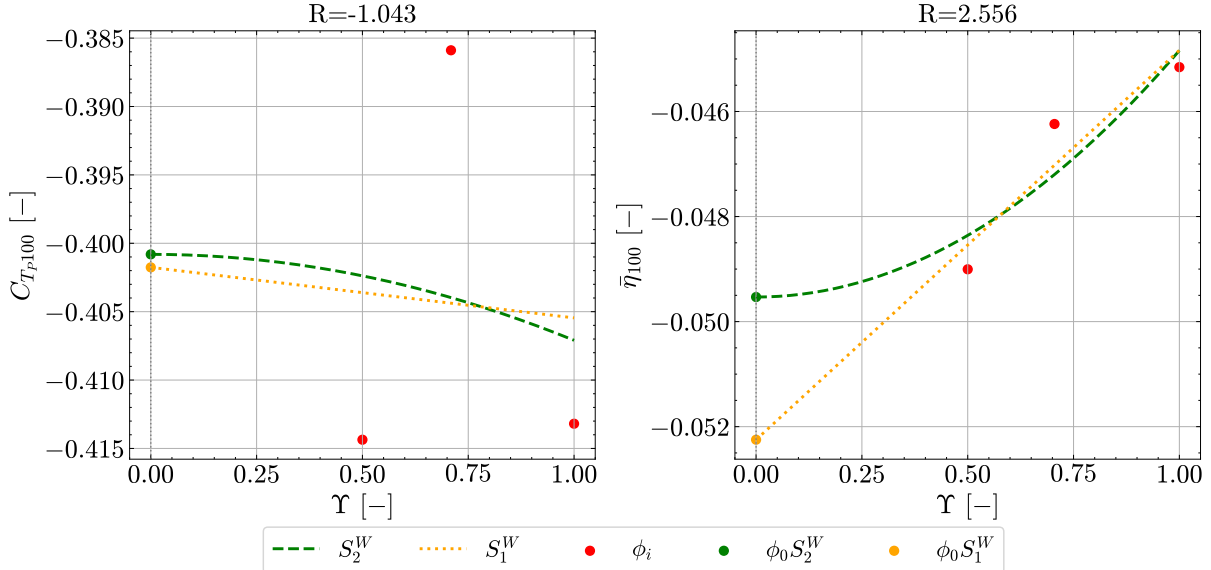


Figure 13: Grid independent solutions for $\bar{\eta}_{100}$ and C_{T_P100} (Non-weighted approach). The left plot shows the mean drag pressure coefficient C_{T_P100} as a function of Υ . The convergence ratio R shows an oscillatory divergence. The right plot presents the mean water level elevation $\bar{\eta}_{100}$ as a function of Υ , in this case a monotonous divergence is observed.

Table 6: Discretization error in percent for C_{T_P100} and $\bar{\eta}_{100}$.

C_{T_P100} [-]	ϕ_1	ϕ_2	ϕ_3	$\bar{\eta}_{100}$ [-]	ϕ_1	ϕ_2	ϕ_3
$\delta_D^{S_1}$ [%]	2.39	4.75	1.45	$\delta_D^{S_1}$ [%]	6.15	11.69	13.58
$\delta_D^{S_2}$ [%]	3.5	4.0	2.13	$\delta_D^{S_2}$ [%]	0.87	6.13	7.93

To yield a converged grid independent solution, one should consider another degree of refinement, as the grid uncertainty may be too high for the coarsest grid. Computing a finer grid, with the same refinement ratio of $\sqrt{2}$, would approximately result in a 46 million cells mesh, which would require substantial computation resources that were not available in the ambit of this project.

4.3.2 Grid independent solution of an array-type quantity

To further quantify the grid independent solution, we applied the method of Oberhage-mann and el Moctar 2019 on an array-type quantity: the wave elevation profile (draw-down) measured at 50 points along the probe line from the experiments (at $y = 21.73$

m). The corresponding experimental data will serve as a reference for validating our simulation results.

Figure 14 shows the non-dimensional drawdown elevation along the hull at $y = 21.73$ m for the three grids detailed in 5 as well as ϕ_0 , the grid independent solution and the discretization error δ_D computed as mentioned in equation 2.10. The grid independent solution ϕ_0 is obtained using the estimator S_2^W , which provides a more conservative estimate than S_{12}^W , but less conservative than S_1^W (see 2.4). It illustrates that the behavior of the secondary wave-field is strongly grid-dependent. The primary wave field exhibits good agreement across all mesh resolutions.

The behavior of 50 points alongside the draw down is the following:

- Monotonic convergence : 2 points
- Monotonic divergence : 15 points
- Oscillatory convergence : 8 points
- Oscillatory divergence : 25 points

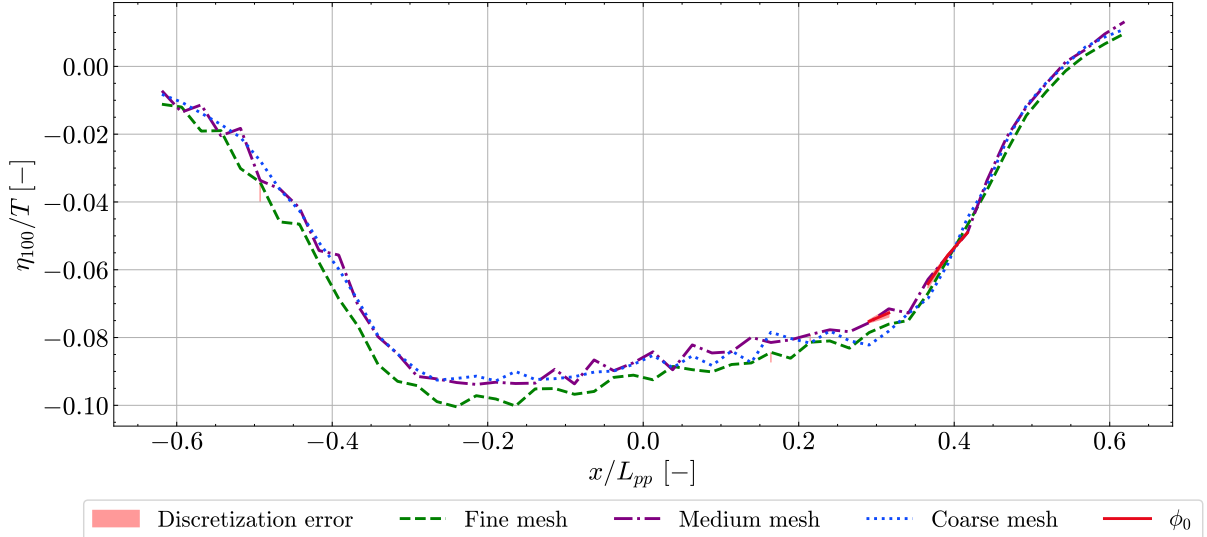


Figure 14: Time-averaged non-dimensional water level elevation η_{100}/T , cut at $y = 21.73$ m as a function of the non-dimensional x-coordinate x/L_{pp} . Fine, Medium, Coarse depict the various meshes. ϕ_0 is the grid independent solution, which is extrapolated from 50 points along the wave-cut only when monotonic convergence is obtained.

Overall, the results indicate that the secondary wave-field does not converge uniformly across all spatial locations and that its accurate prediction requires sufficiently refined discretization. The predominance of divergence in 40 out of the 50 points suggests that mesh refinement alone may not fully eliminate numerical artifacts, potentially due to the interaction between discretization errors and the complex structure of the reflected or radiated waves.

4.4 Spatial and temporal Fourier analysis

To investigate the various wave lengths along the secondary wave-field, a spatial Fourier Transform is performed using the python package `numpy` and the function `numpy.fft.rfft`.

The spatial analysis presented in figure 15 shows the normalized amplitude of the Fourier transform as a function of λ , the wave lenght in meters over three different meshes, ranging from fine to coarse. It highlights the presence of several wavelength components whose amplitudes are significantly influenced by the mesh resolution. In particular, finer meshes tend to resolve shorter wavelengths with higher accuracy.

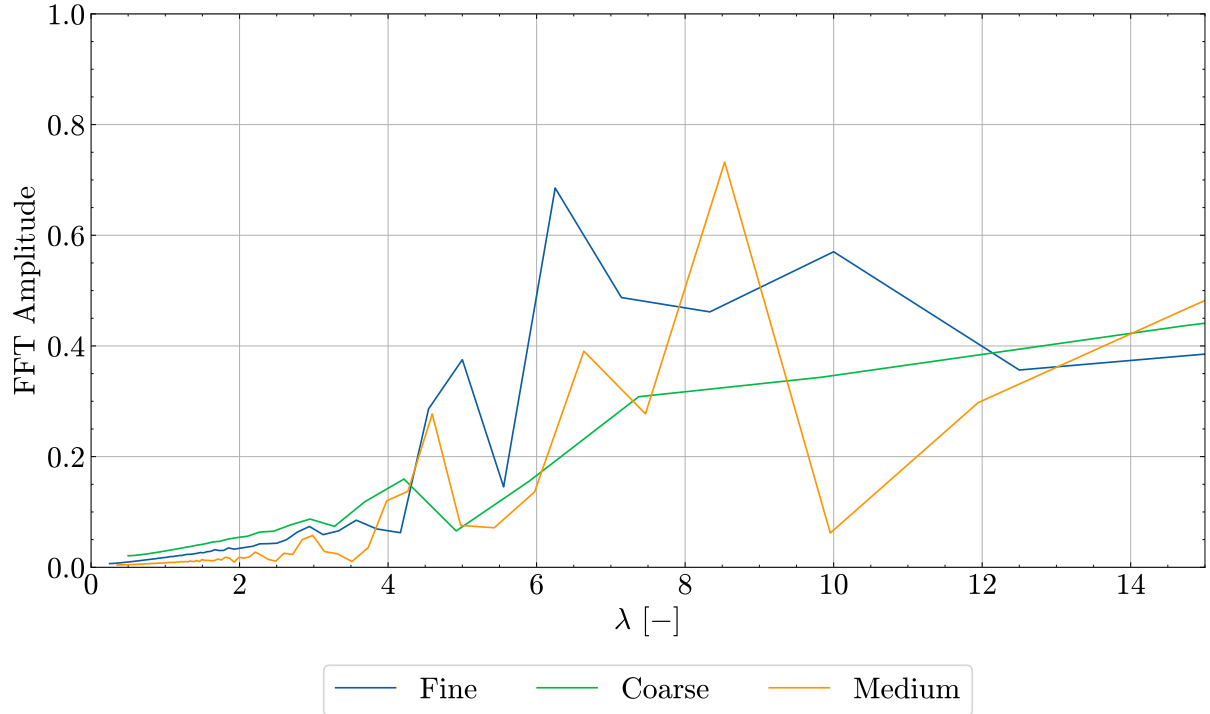


Figure 15: FFT amplitude as a function of λ , the wave length in meters. The mesh resolution significantly affects the secondary wave field.

To further characterize the influence of the mesh resolution on the dynamic response, a temporal Fast Fourier Transform (FFT) was performed along 50 points along the wave-cut. This analysis aims to identify whether specific temporal frequencies are consistently present across meshes or whether certain components are artificially introduced by discretization errors.

The Figure 16 shows the normalized temporal FFT amplitude as a function of frequency and the non-dimensional coordinate x/L_{pp} for the three mesh resolutions. The coarse mesh displays higher amplitudes across a wider frequency range, suggesting the presence of numerical noise and spurious temporal oscillations due to a large spatial resolution. In contrast, the fine mesh concentrates most of the energy below 0.1 Hz and exhibits a more uniform spectral distribution along the hull, indicating improved temporal stability. The medium mesh presents intermediate characteristics, with some residual higher-frequency content but reduced variability compared to the coarse mesh. Additionally, the secondary waves located in the regions $x/L_{pp} = [-0.1, 0.2] \cup [-0.5, -0.3]$ show unsteady behavior, which is more pronounced in the coarse and medium meshes. As shown in Figure 14, the most unsteady regions correspond to the areas where the majority of the secondary waves are located.

In summary, both the spatial and temporal FFT analyses highlight the strong sensitivity of the secondary wave-field to the mesh resolution. While finer grids allow for a more accurate representation of short wavelengths and reduce spurious temporal oscilla-

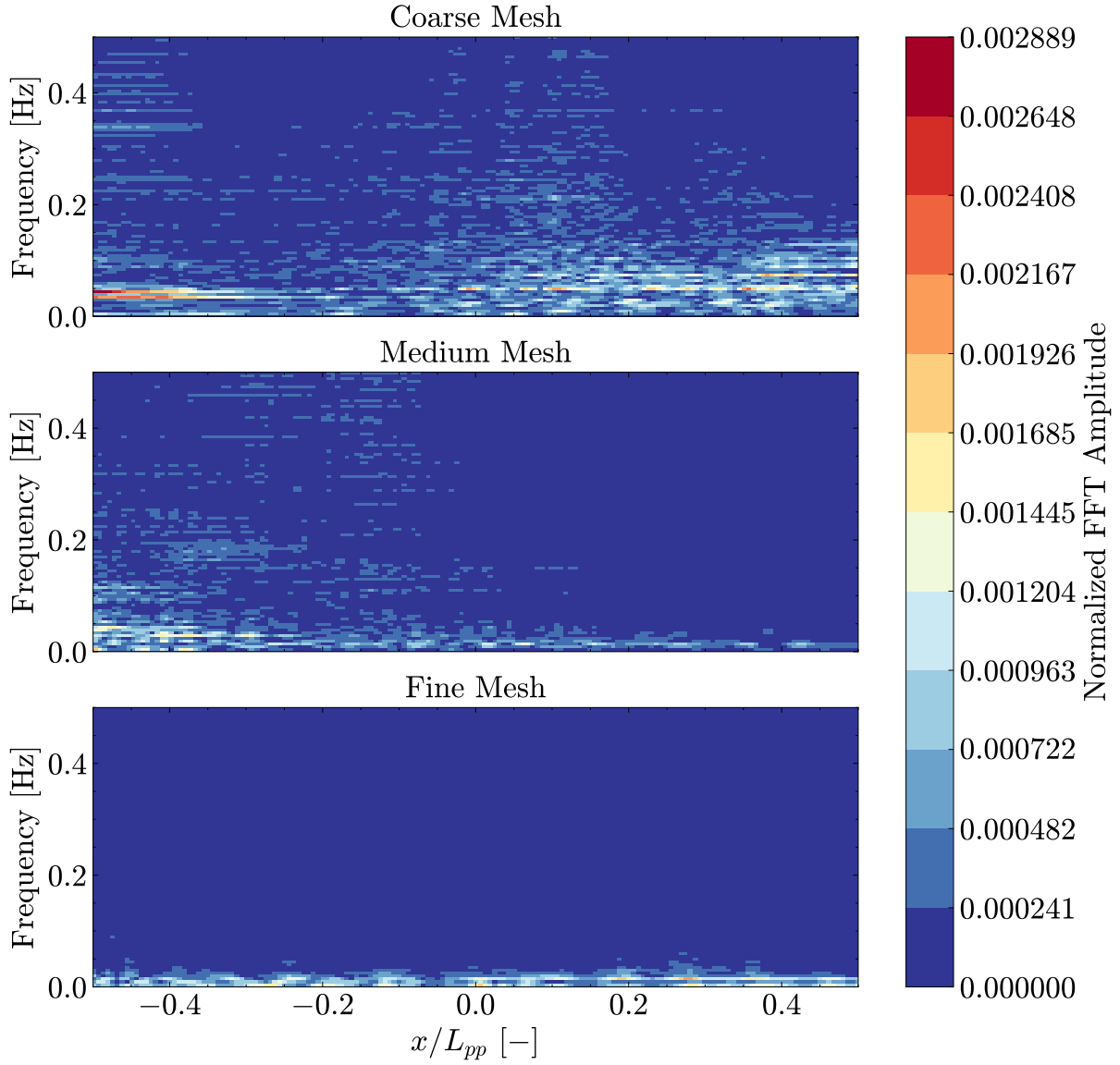


Figure 16: Normalized amplitude of the temporal Fast Fourier Transform (FFT) as a function of frequency (in Hz) and the non-dimensional longitudinal coordinate x/L_{pp} .

tions, some areas remain difficult to fully resolve, particularly in the regions with strong secondary wave activity. However, the limited sampling rates, both temporal and spatial along the wave-cut, may have hindered a more detailed characterization of the spectral content, especially in zones where the wave dynamics are highly localized. A denser sampling (provided by finer meshes) could provide further insight into the interplay between spatial discretization and wave generation, and would be a valuable extension to this analysis.

4.5 Validation

To ensure the accuracy of the numerical results, a validation was performed against reference data. The comparison focuses on the free-surface elevation and was carried out in three stages. First, a qualitative assessment was made using a photograph taken during the experimental campaign. This was followed by a second qualitative analysis

based on measured data, and finally by a quantitative evaluation using the normalized root mean square error.

Figure 17 presents an overview of both experimental and numerical data. Both figures show a good agreement between the wave field, except for the secondary wave-field which seems over exaggerated in the numerical simulation.

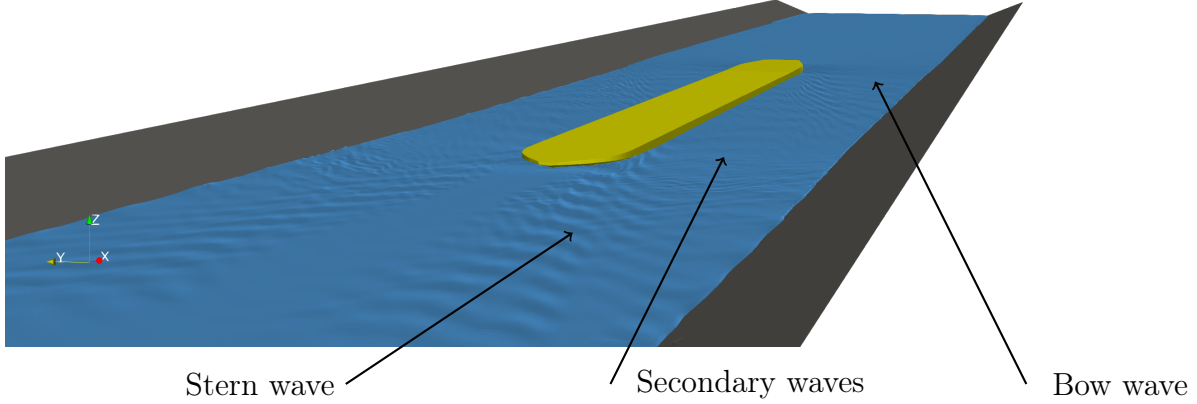


Figure 17: Comparison of the computed free surface ($\alpha = 0.5$) and the real wave-field (bottom). The multiple components of the wave-field are visible such as the stern and bow waves as well as the secondary waves.

Figure 18 illustrates the experimental setup. The ship is positioned along the canal centerline, while the ultrasonic probe used to record wave elevations is located partway up the canal bank.

Figure 19 presents a comparison of the draw down wave computed experimentally and

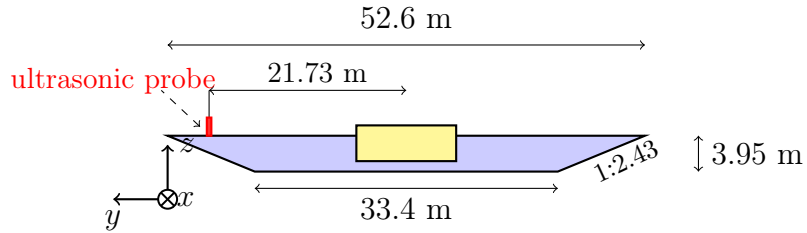


Figure 18: Schematic of the experimental setup with the ship positioned at the centerline of the canal. The ultrasonic probe is placed near the canal bank, 21.73 m from the bow, to record the ship-generated wave elevations.

numerically. The overall shape of the wave is captured; however, an error of approximately 20% remains within the range $\eta/T \in [-0.35, 0.35]$. The amplitude of the secondary waves differs significantly, being approximately 1 cm in the experiment, whereas the numerical results indicate an amplitude of about 20 cm. The combined effect of trim and propeller suction is also more pronounced in the experimental data from $\eta/T = -0.3$ to $\eta/T = -0.05$.

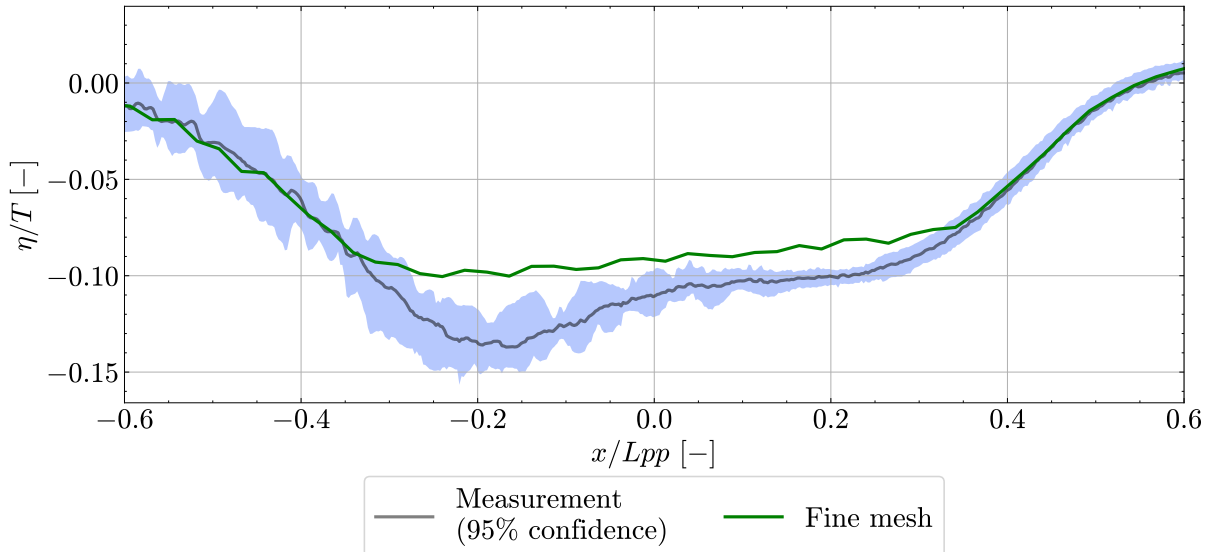


Figure 19: Non-dimensional free surface elevation η as a function of the non-dimensional x coordinate.

To quantify the error properly, a Normalized Root Mean Square Error (NRMSE) approach was applied:

$$\text{NRMSE} = \frac{\sqrt{\frac{1}{N} \sum_{i=1}^N (\eta_i^{\text{num}} - \eta_i^{\text{exp}})^2}}{\max(\eta^{\text{exp}}) - \min(\eta^{\text{exp}})} \quad (4.3)$$

Where N is the number of data points, η_i^{num} , η_i^{exp} denote the free-surface elevation computed using CFD and the experimental value, respectively.

Figure 20 presents the NRMSE approach previously described. It shows that the model struggles to fully capture the pressure field as well as the secondary wave structures. The finest mesh shows better agreement with the experimental data, which encourages us to perform finer computations.

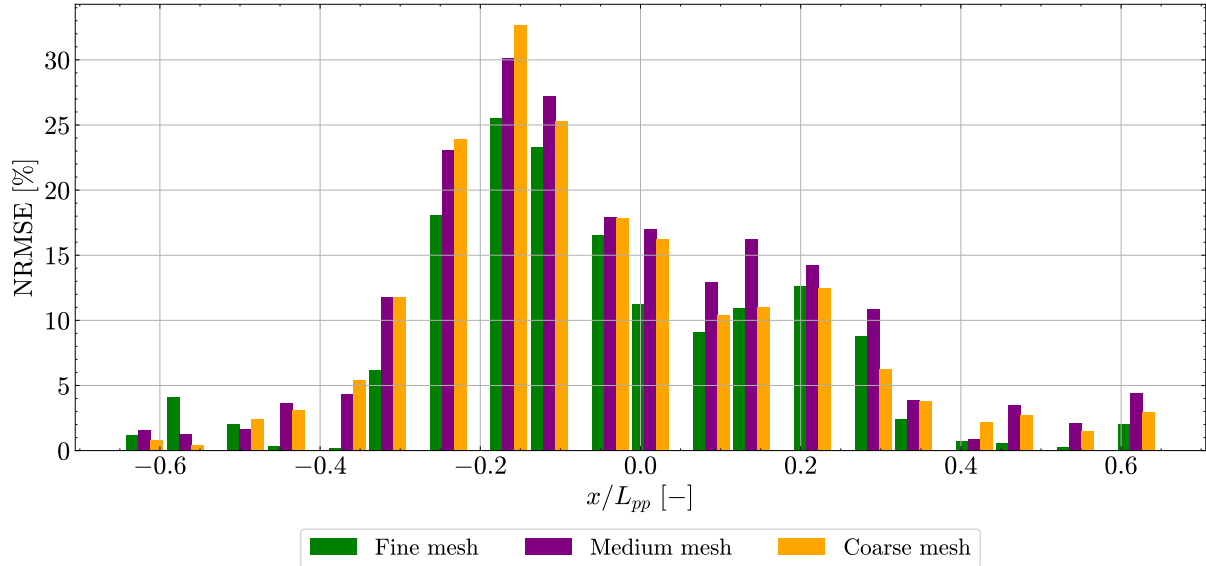


Figure 20: NRMSE as a function of the non-dimensional x coordinate. The values were computed at 20 points along the draw down, leading to mean NRMSE values of: $\text{NRMSE}^{\text{Fine}} = 8.17\%$, $\text{NRMSE}^{\text{Medium}} = 10.68\%$, and $\text{NRMSE}^{\text{Coarse}} = 10.18\%$.

Despite these discrepancies, the overall agreement in the primary wave shape is encouraging and demonstrates the potential of the numerical approach. With further refinement and improved modeling of propeller and trim effects, the simulation can be expected to achieve an even closer match to the experimental observations. The smallest mesh cell (0.06 m) was still $\sim 10\times$ larger than the amplitude of secondary waves ($\sim 0.005\text{--}0.01$ m), highlighting the need for finer meshes to resolve those small waves.

5 Conclusion

In the present study, we performed a verification and validation exercise considering the numerical simulation of ship-induced waves in confined environments. For this purpose we applied the grid uncertainty estimation procedure by Oberhagemann and el Moctar 2019 to the case introduced by Göbel et al. 2023. We performed RANS based multi-phase simulations using the open-source CFD toolbox OpenFOAM. We generated three successively refined grids and estimated the grid uncertainty for both an integral scalar quantity, the ship resistance, and an array-type quantity, the free-surface elevation in the vicinity of the ship. The findings of our study can be summarized as follows:

- Coarse meshes are generally adequate for capturing the primary wave field, with little variation in the dominant wave components across grids. However, the secondary waves are highly sensitive to discretization and are better resolved as the mesh is refined.
- Grid convergence was not achieved for several scalar and array-type quantities. Even with mesh refinement, significant time variations persisted, underlining the inherent challenges in simulating unsteady free-surface flows.
- Interpolation errors arise due to the shifting cell locations along the drawdown wave between grids, introducing additional uncertainty when comparing results.
- Spatial spectral analysis confirms that accurate representation of the secondary wavelengths requires finer grids. Temporal spectral analysis further shows that coarse meshes introduce artificial high-frequency oscillations and amplify unsteady behavior, whereas refined meshes more effectively suppress spurious fluctuations and reveal the low-frequency dynamics characteristic of the primary waves.
- Comparisons with experimental data indicate an underestimation of the pressure field, likely due to incomplete modeling of propeller effects and sinkage. This discrepancy reinforces the need for higher spatial resolution to capture the amplitude of secondary waves more accurately.
- As emphasized in Ferziger et al. 2019, modeling errors or input uncertainties remain difficult to quantify and appear to play a significant role in the deviations observed. No rudder or propeller information was available leading to consequential modeling error.

Overall, these results underscore the critical importance of adequate mesh resolution for reliable prediction of complex wave fields and support the use of refined grids in simulations of unsteady free-surface flows.

Future work could include the implementation of a 2-Degrees of Freedom (DoF) algorithm to account for ship dynamic motions (trim and sinkage). Longer simulation times, or alternative numerical schemes may be necessary to better assess convergence behavior and reduce sensitivity to grid resolution.

Additional sensitivity analyses could be performed by independently varying the temporal resolution or adopting higher-order discretization schemes to assess whether the observed grid dependence is primarily spatial or also influenced by time integration accuracy. Finally, a new experimental campaign is planned to gather more experimental data, improving the validation processes.

References

- Brouwer, J., Tukker, J., & van Rijsbergen, M. (2015). Uncertainty analysis and stationarity test of finite length time series signals. *Proceedings of the 4th International Conference on Advanced Model Measurement Technology for the Maritime Industry (AMT)*.
- Dempwolff, L.-C., Melling, G., Windt, C., Lojek, O., Martin, T., Holzwarth, I., Bihs, H., & Goseberg, N. (2022). Loads and effects of ship-generated, drawdown waves in confined waterways - a review of current knowledge and methods. *Journal of Coastal and Hydraulic Structures*, 2, 46. <https://doi.org/10.48438/jchs.2022.0013>
- Descamps, T., Elsayed, O., Bouscasse, B., Lasbleis, M., & Gouin, M. (2025). Validation and verification applied to cfd simulations of ship responses to regular head waves with forward speed. *Ocean Engineering*, 320, 120177. <https://doi.org/https://doi.org/10.1016/j.oceaneng.2024.120177>
- Du, P., Ouahsine, A., Sergent, P., & Hu, H. (2020). Resistance and wave characterizations of inland vessels in the fully-confined waterway. *Ocean Engineering*, 210, 107580. <https://doi.org/https://doi.org/10.1016/j.oceaneng.2020.107580>
- Duró, G., Crosato, A., Kleinhans, M. G., Roelvink, D., & Uijttewaal, W. S. J. (2020). Bank erosion processes in regulated navigable rivers [e2019JF005441 2019JF005441]. *Journal of Geophysical Research: Earth Surface*, 125(7), e2019JF005441. <https://doi.org/https://doi.org/10.1029/2019JF005441>
- Eça, L., & Hoekstra, M. (2009). Evaluation of numerical error estimation based on grid refinement studies with the method of the manufactured solutions. *Computers & Fluids*, 38(8), 1580–1591. <https://doi.org/https://doi.org/10.1016/j.compfluid.2009.01.003>
- Eça, L., & Hoekstra, M. (2014). A procedure for the estimation of the numerical uncertainty of cfd calculations based on grid refinement studies. *Journal of Computational Physics*, 262, 104–130. <https://doi.org/https://doi.org/10.1016/j.jcp.2014.01.006>
- Ferziger, J. H., Peric, M., & Street, R. L. (2019). *Computational methods for fluid dynamics* (4th). Springer. <https://doi.org/10.1007/978-3-319-99693-6>
- Göbel, G., Zentari, L., Brutto, C., & Jankowski, J. (2023). Full scale predictions of ship induced waves in restricted waters with numerical tools -a comparative study.
- Hirt, C. W., & Nichols, B. D. (1981). Volume of fluid (vof) method for the dynamics of free boundaries. *Journal of Computational Physics*, 39(1), 201–225. [https://doi.org/10.1016/0021-9991\(81\)90145-5](https://doi.org/10.1016/0021-9991(81)90145-5)
- Islam, H., & Guedes Soares, C. (2019). Uncertainty analysis in ship resistance prediction using openfoam. *Ocean Engineering*, 191, 105805. <https://doi.org/https://doi.org/10.1016/j.oceaneng.2019.02.033>
- Lataire, E., Vantorre, M., & Delefortrie, G. (2012). A prediction method for squat in restricted and unrestricted rectangular fairways. *Ocean Engineering*, 55, 71–80. <https://doi.org/https://doi.org/10.1016/j.oceaneng.2012.07.009>
- Menter, F. R. (1994). Two-equation eddy-viscosity turbulence models for engineering applications. *AIAA Journal*, 32(8), 1598–1605. <https://doi.org/10.2514/3.12149>
- Nichols, B. D., Hirt, C. W., & Hotchkiss, R. S. (1980). *Sola-vof: A solution algorithm for transient fluid flow with multiple free boundaries* (tech. rep. No. LA-8355). Los Alamos National Laboratory. Los Alamos, NM, USA. <https://www.osti.gov/biblio/5122053>

- Oberhagemann & el Moctar. (2019). An extrapolation method for discretization independent solution of uncertainty quantification procedure for time domain cfd computations. *Submitted to: Ship Technology Research*.
- Pena, B., & Huang, L. (2021). A review on the turbulence modelling strategy for ship hydrodynamic simulations. *Ocean Engineering*, 241, 110082. <https://doi.org/https://doi.org/10.1016/j.oceaneng.2021.110082>
- Pereira, F., Eça, L., & Vaz, G. (2017). Verification and validation exercises for the flow around the kvlcc2 tanker at model and full-scale reynolds numbers. *Ocean Engineering*, 129, 133–148. <https://doi.org/https://doi.org/10.1016/j.oceaneng.2016.11.005>
- Raza, A., Zeng, Q., & Van Hoydonck, W. (2025). Scale effects on nominal wake fraction in shallow water: An experimental and cfd investigation. *Journal of Marine Science and Engineering*, 13(3). <https://doi.org/10.3390/jmse13030619>
- van der Vorst, H. A. (1992). Bi-cgstab: A fast and smoothly converging variant of bi-cg for the solution of nonsymmetric linear systems. *SIAM Journal on Scientific and Statistical Computing*, 13(2), 631–644. <https://doi.org/10.1137/0913035>
- Weller, H., Tabor, G., Jasak, H., & Fureby, C. (1998). A tensorial approach to computational continuum mechanics using object orientated techniques. *Computers in Physics*, 12, 620–631. <https://doi.org/10.1063/1.168744>
- Xing, T., & Stern, F. (2010). Factors of safety for richardson extrapolation. *Journal of Fluids Engineering*, 132(6), 061403. <https://doi.org/10.1115/1.4001771>